

1 **Hydrothermal fluid pressure-temperature drives CO₂ emission and seismicity at** 2 **Campi Flegrei (Italy)**

3

4 G. Chiodini^{1,*}, S. Caliro², R. Avino², G. Bini³, F. Giudicepietro², W. De Cesare², P. Ricciolino², A.
5 Aiuppa⁴, C. Cardellini^{5,1}, Z. Petrillo², J. Selva¹, A. Siniscalchi⁶, S. Tripaldi⁶

6

7 ¹ Istituto Nazionale di Geofisica e Vulcanologia, Sezione di Bologna, via D. Creti 12, 40128
8 Bologna, Italy.

9 ² Istituto Nazionale di Geofisica e Vulcanologia, Sezione di Napoli Osservatorio Vesuviano, via
10 Diocleziano 328, 80124 Napoli, Italy.

11 ³ Institute of Geochemistry and Petrology, ETH Zürich, Clausiusstrasse 25, 8092 Zürich,
12 Switzerland

13 ⁴ Dipartimento di Scienze della Terra e del Mare (DiSTeM), Università degli Studi di Palermo, via
14 Archirafi 22, 90123 Palermo, Italy.

15 ⁵ Dipartimento di Fisica e Geologia, Università degli Studi di Perugia, via Pascoli snc, 06123
16 Perugia, Italy.

17 ⁶ Dipartimento di Scienze della Terra e Geoambientali Università degli Studi di Bari - Aldo Moro,
18 via Edoardo Orabona, 4, 70125 Bari, Italy.

19

20 *corresponding author: giovanni.chiodini@ingv.it

21

22 **Highlights**

- 23 ■ Gas-geoindicators indicate an escalation of the hydrothermal P-T Campi Flegrei
- 24 ■ Pressurization causes increase of the CO₂ emission at Solfatara (up to 5000 t/d)
- 25 ■ Increasing P-T triggers low magnitude earthquakes within the hydrothermal system

26

27 **Abstract**

28 Fluids supplied by stored magma at depth are causal factors of volcanic unrest, as they can cause
29 pressurization/heating of hydrothermal systems. However, evidences for a link between
30 hydrothermal pressurization, CO₂ emission and volcano seismicity have remained elusive. Here, we
31 use recent (2010-2020) observations at Campi Flegrei caldera (CFc) to show hydrothermal pressure,
32 gas emission and seismicity at CFc share common source areas and well-matching temporal
33 evolutions. We interpret the recent escalation in seismicity and surface gas emissions as caused by
34 pressure-temperature increase at the top of a vertically elongated (0.3-2 km deep) gas front. Using
35 mass (steam) balance considerations, we show hydrothermal pressurization is causing energy

36 transfer from the fluids to the host rocks, ultimately triggering low magnitude earthquakes within a
37 seismogenic volume containing the hydrothermal system. This mechanism is probably common to
38 other worldwide calderas in similar hydrothermal activity state.

39

40 **Keywords**

41 Volcanic unrest, hydrothermal systems, Campi Flegrei, fumarole compositions, CO₂ emission,
42 volcano seismicity

43

44 **1. Introduction**

45 The injection, ascent, storage and surface release of deep fluids in the upper crust are widespread
46 phenomena in nature, and are recurrent drivers of geological catastrophes. Fluid pressure increase in
47 the upper crust can trigger seismicity reducing the effective normal stress on fault planes (e.g.
48 (Hubbert and Rubey, 1959; Sibson, 1992; Miller, 2013), and the recurrently observed co-seismic
49 variations in gas flux and composition (Fischer et al., 2017; Girault et al., 2018; Chiodini et al.,
50 2020) are clear hints for a cause-effect link between fluids and earthquakes. It is also well-
51 established that artificial fluid injection in the subsurface, and the consequent fluid pressure
52 increase, can lead to seismicity (Ellsworth, 2013; Keranen and Weingarten, 2018).

53 Volcanoes make no exception, the most notable example being that of Mammoth Mt (California),
54 when the sudden surface burst (in 1990) of huge amounts of volcanic-hydrothermal CO₂ associated
55 to a seismic crisis killed a large portion of the forest (Farrar et al., 1995; Sorey et al., 1998), and
56 repeated increases in diffuse CO₂ emissions accompanied seismic swarms in the subsequent years
57 (Lewicki et al., 2014; Hotovec-Ellis et al., 2018; Pfeiffer et al., 2018; Werner et al., 2014).

58 Volcanoes are especially suitable natural laboratories for investigating fluid flow - pressure -
59 earthquake associations, because robust and relatively continuous geochemical and geophysical
60 datasets are available. One aspect that is especially relevant to restless volcanoes is that injected
61 fluids are generally hot and H₂O-rich so that, upon ascent, can interact with, and condense into,
62 hydrothermal aquifers: the heating and volumetric expansion of the hosting rocks that result from

63 condensation of such magmatic steam is a potential additional seismicity driver during volcanic
64 unrest (Chiodini et al., 2015).

65 The relations among hydrothermal temperature-pressure, fluid flow and earthquakes are here
66 investigated at Campi Flegrei (CFc, Fig. 1a), a restless resurgent caldera formed ~ 39 kyrs ago by
67 the largest caldera-forming eruption in Europe in the last 200 kyrs (Costa et al., 2012). CFc exhibits
68 (since the 1950s) repeated inflation periods (Orsi et al., 1999; Del Gaudio et al., 2010) and seismic
69 crises, which have worried the scientific community as much to suggest an eruption is approaching
70 (Kilburn et al., 2017; Selva et al., 2012). The CFc is undergoing since 2004 a new inflation phase
71 (total maximum vertical displacement of ~ 0.75 m by the time of writing), associated with frequent
72 shallow seismicity, part of which interpreted as originating from fluid transfer processes (Bianco et
73 al., 2004; Saccorotti et al., 2007; Chiodini et al., 2017a; D'Auria et al., 2011; Giudicepietro et al.,
74 2020). At the same time, large compositional variations are being observed in the fumarolic
75 effluents (Caliro et al., 2014; Chiodini et al., 2016), and marked flux increases are being registered
76 in hydrothermal CO₂ release from both fumarolic vents (Tamburello et al., 2019) and soil diffuse
77 degassing structures (Cardellini et al., 2017). The escalating CO₂ emissions, and the concomitant
78 compositional changes in the fumaroles, have been interpreted as signs that magma degassing at
79 depth may have reached a critical condition in which heating and pressurization of the shallower
80 CFc hydrothermal system is occurring at accelerating rate (Caliro et al., 2014; Chiodini et al., 2015;
81 Chiodini et al., 2016). In 2012, the evolution of the monitored geophysical and geochemical
82 parameters induced the Italian Civil Protection (DPC) to raise the CFc alert level from green (calm)
83 to yellow (attention).

84 Here, we characterise the recent pressure-temperature (P-T from here on) evolution in the CFc
85 hydrothermal system, as inferred from geochemical modelling of fumarolic compositions, and to
86 explore its temporal link with the rates of deeply derived CO₂ emissions and seismicity. To this
87 aim, our multidisciplinary analysis combines results for the chemical compositions of the CFc
88 fumaroles with a set of variables relates to the gas emission, and the earthquakes. We exclude from

89 our analysis the deformation signals, as their main source area is thought to be deeper than the
90 hydrothermal system this work is focussed on (3-4 km; Amoruso et al., 2014a; 2014b).
91 Geochemical data (fumarolic compositions and CO₂ fluxes) refer to the hydrothermal sites of
92 Solfatara and Pisciarelli (Fig. 1). Solfatara, a tuff cone formed about 4 ka ago (Smith et al., 2011), is
93 the most active degassing zone of the CFC, being site of numerous fumarolic vents and of a
94 widespread soil diffuse degassing of hydrothermal-volcanic CO₂ (Chiodini et al., 2001; Cardellini et
95 al., 2017; Fig. 1b). The most recent CO₂ flux measurements performed over the entire zone identify
96 a ~ 1 km² wide area diffusively emitting deeply derived CO₂ (the so called Solfatara Diffuse
97 Degassing Structure, Solfatara DDS, Fig. 1b). The typical CO₂ flux sustained by the DDS was
98 1000-2000 t d⁻¹ in 2014-2016 period (Cardellini et al., 2017). Significant amounts of CO₂ are also
99 emitted by fumarolic vents, the most active of which are located in the eastern slope of the Solfatara
100 cone (Pisciarelli vents, CO₂ emission up to 600 t d⁻¹ in 2019 (Tamburello et al., 2019) and inside the
101 Solfatara depression (BG and BN vents, CO₂ emission up to ~ 300 t d⁻¹ in 2013; Aiuppa et al.,
102 2013; Pedone et al., 2014; Fig. 1b).
103 After a description of the evolution over time of different parameters we attempt at an integrated
104 analysis aimed at understanding the impact of hydrothermal fluid P-T changes on earthquakes
105 occurrence and fluid emissions.

106

107 **2. Material and methods**

108 **2.1. Used databases**

109 The databases used in this work (Supplementary Data File S1) are here briefly described.

110 **2.1.1. Chemical compositions of Solfatara fumaroles.**

111 The main and hottest fumaroles of Solfatara, BG (T=150-165°C) and BN (T 140-150°C) (Fig. 1b),
112 have been systematically sampled since 1983 and 1995, respectively. The dataset includes the
113 temperature and chemical compositions (H₂O, CO₂, Ar, N₂, H₂, CH₄ and CO) of gas samples taken

114 and analysed with similar procedures, from 1983 to 2020 (see Caliro et al. (2007) and Cioni and
115 Corazza (1981) for the sampling and analytical methods). This Solfatara fumarolic fluid database is
116 unique for the large number of samples (671), for its continuity (~ 35 years of observations) and for
117 the homogeneity of the sampling and analytical methods used. Different laboratories contributed to
118 this database: the laboratories of CNR of Pisa that started the work at the beginning of 1980's; the
119 laboratory of University of Perugia that analysed the gas samples in the middle 1990's; and the fluid
120 geochemistry laboratory of Osservatorio Vesuviano from 1998 to 2020.

121

122 ***2.1.2. Diffuse CO₂ flux from the Solfatara crater target area.***

123 During April 2004 - October 2020, 149 soil CO₂ flux campaigns have been performed inside the
124 Solfatara crater. In total, the dataset consists of 9315 measurements performed with the
125 accumulation chamber method (Chiodini et al., 1998) over a grid of 63 points whose location
126 remained unchanged during the period (Fig. 1b). The data are reported in monthly surveillance
127 reports of Osservatorio Vesuviano for the Civil Defence of Italy
128 (<http://www.ov.ingv.it/ov/it/bollettini/275.html>). The results of the first 50 campaigns have already
129 been published (Granieri et al., 2009), while the remaining are here reported for the first time. For
130 each campaign, we computed the total CO₂ output (FCO₂ in t d⁻¹) from the target area (Fig. 1b).
131 The FCO₂ and its uncertainty were computed by applying a geostatistical method based on
132 sequential Gaussian simulation (sGs; Cardellini et al., 2003) to the soil CO₂ fluxes of the 149
133 campaigns. Specifically, we used the *sgsim* algorithm (GSLIB software library; Deutsch and
134 Journel, 1998). The CO₂ flux has been simulated on a of 4 × 4 grid m starting from variogram
135 models fitting the experimental variograms of the normal scores of the CO₂ flux (for further details
136 see Cardellini et al., 2003). For each campaign, 200 simulations were realised and the total CO₂
137 release was computed by summing the products of the simulated CO₂ flux value at each grid cell by
138 the cell surface. The mean total CO₂ flux and its standard deviation, computed from the 200

139 realizations, are taken as FCO₂ and its uncertainty for each campaign. As an example,
140 Supplementary Fig. S1 illustrates the CO₂ flux map obtained considering at each location the mean
141 of the CO₂ fluxes measured in the 149 campaigns. The target area to which each FCO₂ estimate
142 refers to (coloured area in Supplementary Fig. S1) was limited to the area within the outermost
143 measuring points, in order to avoid uncertainties related to extrapolations to un-sampled zones.

144

145 ***2.1.3. Diffuse CO₂ flux from the Solfatara DDS.***

146 This dataset includes the total CO₂ output by diffuse degassing at Solfatara (FCO₂-DDS) from 1998
147 to 2016 estimated from soil CO₂ flux measurements covering an area of 1.4 km² which includes
148 Solfatara crater and Pisciarelli areas (Fig. 1b; Cardellini et al., 2017). The soil CO₂ fluxes were
149 measured in 30 surveys using the accumulation chamber method (Chiodini et al., 1998) and the
150 total CO₂ output was estimated applying a geostatistical method based on sGs (for further details
151 see Cardellini et al., 2017).

152

153 ***2.1.4. CO₂ fluxes from Pisciarelli vents.***

154 This dataset is composed of twenty-one measurements of the CO₂ flux from the Pisciarelli vents
155 performed by different authors during 2012-2019 (Aiuppa et al., 2015; Aiuppa et al., 2013; Pedone
156 et al., 2014; QueiBer et al., 2017; Tamburello et al., 2019). Measurement methods are different and
157 include: tunable diode laser absorption spectroscopy (Pedone et al., 2014), differential absorption
158 lidar (Aiuppa et al., 2015), laser remote-sensing spectrometry (LARSS; QueiBer et al., 2017), multi-
159 component gas analyzer system (MultiGAS; Aiuppa et al., 2013; Tamburello et al., 2019). The
160 reader is referred to the original articles for the details on these different techniques.

161

162 ***2.1.5. Fumarolic tremor at Pisciarelli.***

163 The fumarolic tremor is a continuous seismic signal recorded in the vicinity of the Pisciarelli
164 fumaroles, currently the largest of the CFc. To record this signal, a seismic station was installed in
165 2010 about 8 m away from the main fumarolic vent. The fumarolic tremor, analyzed in previous
166 studies (Chiodini et al., 2017b; Giudicepietro et al., 2019; Giudicepietro et al., 2020), is polarized
167 in the vertical direction and characterized by a spectral peak at around 10 Hz. To represent the
168 temporal evolution of the tremor amplitude, the Real-time Seismic-Amplitude Measurement
169 (RSAM; Endo and Murray, 1991) was calculated on 30-minute windows of the vertical component
170 signal, filtered in 5 -15 Hz frequency band.

171

172 **2.1.6. Air CO₂ concentrations at Pisciarelli.**

173 Since April 2007, an automatic station measures soil temperature, soil CO₂ fluxes, and CO₂
174 concentrations in air, at 40 cm height, 20 m downwind of the main Pisciarelli vent (Chiodini et al.,
175 2017b). The April 2007-October 2020 daily air CO₂ concentrations are systematically higher than in
176 ambient air (1000-5000 ppm vs ~ 400 ppm) due to persistent fumigation from the fumarolic plume.

177

178 **2.1.7. Earthquakes**

179 We used the CFc earthquake locations available in the public-access INGV- Osservatorio
180 Vesuviano database
181 (<http://sismolab.ov.ingv.it/sismo/index.php?PAGE=SISMO/last&area=Flegrei>). Hypocentral
182 locations were obtained using a 1D layered velocity model. The dataset consists of 2026 located
183 earthquakes with magnitude (Md) ranging between -1.1 and 3.3, representing about 47% of the total
184 number of CFc earthquakes recorded by the INGV-Osservatorio Vesuviano permanent seismic
185 network between January 2004 and October 2020. Seismicity is mostly concentrated in the
186 Solfatara-Pisciarelli area (Fig. 1a) at relatively shallow depth and the magnitude of the events is
187 generally low with only 16 events with $2.0 \leq Md \leq 3.3$. From 2005 to 2012, earthquakes occurred

188 mainly in swarms. Since 2012-2013, their occurrence rate has increased over time, both as swarms
189 and as single events, with single events becoming more frequent in the last 2 years.

190

191 **3. Results and Discussion**

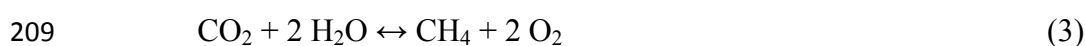
192 **3.1. Pressure-temperature ge indicators based on fumarole compositions**

193 Since 1984, the Solfatara compositional database was used to derive the T-P conditions of the
194 feeding system (e.g., Cioni et al., 1984; Chiodini et al., 1996; Caliro et al., 2007; Chiodini et al.,
195 2015; Chiodini et al., 2016). Recently, two different geochemical approaches have lead to
196 contrasting results and different implications for the current CFC unrest, which has been interpreted
197 as either driven by pressurization of the CFC system (Chiodini et al., 2015; Chiodini et al., 2017a),
198 or associated with a general depressurization of the hydrothermal system (Moretti et al., 2017) (Fig.
199 2). We refer to the two approaches, which stand on different model assumptions, as the *no-*
200 *condensation* (Moretti et al., 2017) and *vapour-liquid coexistence* (Chiodini et al., 2015) models.

201

202 **3.1.1. The no-condensation model**

203 Moretti et al. (2017) applied a model originally developed by Chiodini et al., (1996) and then
204 refined by Chiodini and Marini (1998). The geobarometric and geothermometric relations are
205 derived considering the formation reactions of H₂, CO and CH₄ from the main species H₂O and
206 CO₂:



210 whose equilibrium constants are expressible as:

$$211 \quad \log K_{\text{H}_2} = \log f_{\text{H}_2} + 1/2 \log f_{\text{O}_2} - \log f_{\text{H}_2\text{O}} \quad (4)$$

$$212 \quad \log K_{\text{CO}} = \log f_{\text{CO}} + 1/2 \log f_{\text{O}_2} - \log f_{\text{CO}_2} \quad (5)$$

213
$$\log K_{\text{CH}_4} = \log f_{\text{CH}_4} + 2 \log f_{\text{O}_2} - \log f_{\text{CO}_2} - 2 \log f_{\text{H}_2\text{O}} \quad (6)$$

214 where $\log K_{\text{H}_2} = -12707/T + 2.548$, $\log K_{\text{CO}} = -14955/T + 5.033$ and $\log K_{\text{CH}_4} = -42007/T + 0.527$
 215 (thermodynamic data from Stull et al. (1969)). Suitable combinations of equations 4, 5 and 6 allow
 216 to eliminate the $\log f_{\text{O}_2}$ variable and to derive the following geothermometric and geobarometric
 217 functions:

218
$$T = -2248 / (\text{Log } X_{\text{CO}}/X_{\text{CO}_2} + \text{Log } X_{\text{H}_2\text{O}}/X_{\text{H}_2} - 2.485) \quad (7)$$

219
$$\text{Log } P_{\text{H}_2\text{O}} = (19.605 - \text{Log } (X_{\text{CO}}^4/(X_{\text{CH}_4} \times X_{\text{CO}_2}^3)) - 17813/T)/2 \quad (8)$$

220 where the equimolar ratios of the measured fumarolic molar fractions (X_i) are assumed equal to the
 221 fugacities ratios and $P_{\text{H}_2\text{O}} \sim f_{\text{H}_2\text{O}}$.

222 Finally considering the Dalton law,

223
$$P_{\text{CO}_2} = P_{\text{H}_2\text{O}} X_{\text{CO}_2} / X_{\text{H}_2\text{O}} \quad (9)$$

224
$$P_{\text{tot}} \sim P_{\text{CO}_2} + P_{\text{H}_2\text{O}}. \quad (10)$$

225 Relevant assumptions of this approach are: (i) the redox conditions are internally fixed within the
 226 $\text{H}_2\text{O}-\text{CO}_2-\text{H}_2-\text{CO}-\text{CH}_4$ gas system, an assumption that implies that CH_4 equilibrates at the same T-
 227 P conditions as the kinetically faster species H_2 and CO (Giggenbach, 1987); (ii) no secondary
 228 processes affect H_2O (condensation and/or water addition). Because the contrasting results with the
 229 model of Chiodini et al. (2015) strongly depends on this last assumption, we name the model used
 230 by Moretti et al. (2017) as the *no-condensation* model.

231

232 **3.1.2. The vapor-liquid coexistence model**

233 Caliro et al. (2007) considering the carbon isotopic exchange reaction between CO_2 and CH_4 ,
 234 demonstrated that the CH_4/CO_2 ratio reflects temperatures (360-430°C) much higher than those
 235 returned by the $\text{H}_2/\text{H}_2\text{O}$ and CO/CO_2 ratios (200-250°C). Furthermore, starting from early 2000's,
 236 macroscopic evidences suggested the occurrence of secondary processes (i.e. steam condensation)
 237 affecting the fumarolic H_2O content: (i) the almost continuous increase in the incondensable gas
 238 fraction relative to water (Chiodini et al., 2015); (ii) a systematic increase of the CO/CO_2 ratio (an

239 indicator of hydrothermal temperature, and condensation is very efficient to heat a hydrothermal
 240 system); (iii) the pervasive circulation of condensates underneath Solfatara crater, and in particular
 241 close to the main fumaroles BG and BN (Bruno et al., 2007; Byrdina et al., 2014; Gresse et al.,
 242 2017); (iv) the formation of a strong boiling pools of condensates and repeated episodes of
 243 liquid/mud emission at Pisciarelli (Chiodini et al., 2015).

244 In order to avoid the effects of these secondary processes affecting H₂O, and in order to exclude
 245 CH₄ from the model, Chiodini et al. (2015) derived T-P functions from equations 4 and 5 based on
 246 equimolar ratios between incondensable gases (H₂, CO, CO₂). The derivation of the
 247 geothermometric and geobarometric function was possible considering (i) f_{H₂O} fixed by the vapour-
 248 liquid coexistence and (ii) f_{O₂} as a function of the temperature. Redox conditions of Solfatara gases
 249 were assumed to be controlled by a typical redox buffer for hydrothermal system (DP buffer;
 250 D'Amore and Panichi, 1980) , log f_{O₂} = 8.20 - 23643/T). According to Chiodini and Marini (1998),
 251 an alternative f_{O₂}-T function applicable to Solfatara fumarolic gases is the ‘Campanian Volcanoes’
 252 buffer (CV, log f_{O₂} = 7.75 - 23169/T). The correspondent geothermometric relations are:

$$253 \quad T = 3133.5 / (0.933 - \text{Log } X_{\text{CO}}/X_{\text{CO}_2}) \quad (11)$$

254 valid for redox conditions controlled by the DP relation, and

$$255 \quad T = 3370.5 / (1.158 - \text{Log } X_{\text{CO}}/X_{\text{CO}_2}) \quad (12)$$

256 when considering the CV redox buffer.

257 The geobarometric functions are:

$$258 \quad \text{Log } P_{\text{H}_2\text{O}} = 5.510 - 2048/T \quad (13)$$

259 where the water pressure is assumed equal to water fugacity of saturated vapor (i.e. vapor-liquid
 260 coexistence for pure water (Giggenbach, 1980)),

$$261 \quad \text{Log } P_{\text{CO}_2} = 3.025 + 201/T - \text{Log } X_{\text{H}_2}/X_{\text{CO}} \quad (14)$$

262 derived by a linear combination of equations 4 and 5, and

$$263 \quad P_{\text{tot}} \sim P_{\text{CO}_2} + P_{\text{H}_2\text{O}}. \quad (15)$$

264 Use of either the DP or the CV f_{O_2} -T relation results into different P-T estimations. In agreement
265 with Chiodini et al. (2015), we use the DP option (equation 11) that, for the post 2010 period
266 considered in this work (see Fig. 6), outputs T values from 218°C to 267°C and P from 27 to 60 bar;
267 while the alternative equation 12 (CV buffer) returns higher T and P values (238°C - 287°C, 37 bar
268 - 78 bar). We stress, however, that these systematic differences do not affect the results and
269 considerations of our work that is based on the relative variation of the normalised T-P values that
270 are practically the same for both the DP and CV estimations.
271 We will refer to this model as the *vapour-liquid coexistence* model.

272

273 **3.1.3. Temperature-Pressure estimations**

274 The T-P estimates, derived by the two models for the entire Solfatara fumaroles' database, are
275 contrasted in the chronograms of Fig. 2.

276 Even tough, any model can not be considered completely reliable because it is necessarily based on
277 some a-priori assumptions, the *no-condensation model* is certainly not reliable because the total
278 estimated pressures ($P_{tot} = P_{H_2O} + P_{CO_2}$) for the post-2015 samples are impossible as systematically
279 below atmospheric pressure (<1 bar, Fig. 2b).

280 The reliability of the *vapour-liquid coexistence* model is tested below by comparing the inferred P-
281 T conditions with different independent fluid flow related variables, and with the earthquake
282 occurrence at CFc.

283

284 **3.2. Fluid flow related (FFR) variables**

285 Figures 3a, b ,c, d and e are chronograms of the available FFR variables that we take as proxies for
286 the CO₂ degassing regime of the Solfatara-Pisciarelli area. In particular the CO₂ flux (FCO₂, Fig.
287 3a) from the Solfatara target area (see Fig. 1b) and the total CO₂ flux from the entire Solfatara DDS
288 (FCO₂-DDS, Fig. 3b; Cardellini et al., 2017) are representative of the diffuse emission. Numerous

289 FCO₂ data (149) are available for the entire observation period (2004-2020) while FCO₂-DDS
290 measurements are less frequent (Cardellini et al., 2017) and not available since 2017.
291 The CO₂ flux from Pisciarelli vents (Fig. 3c; Tamburello et al., 2019), the fumarolic tremor at
292 Pisciarelli (RSAM, Fig. 3d) and the CO₂ concentrations in air at Pisciarelli (air CO₂, Fig. 3e) are
293 taken as proxies of the vent emission in the area. Although not direct flux measurements, RSAM
294 and air CO₂ are almost continuously acquired, and their temporal fluctuations have previously been
295 shown to scale with the intensity of hydrothermal activity at Pisciarelli (Fig. 4; Chiodini et al.,
296 2017b; Giudicepietro et al., 2019; Giudicepietro et al., 2020).

297

298 **3.3. 2004-2020 earthquakes occurrence at CFc**

299 We refer here to the earthquakes occurred at CFc from 2004 to October 2020 (Fig. 1a) whose
300 locations and magnitudes are available in public databases of the Osservatorio Vesuviano
301 (<http://www.ov.ingv.it/ov/it/banche-dati.html>; see Material and Methods). It is worth to note that
302 the events concentrate underneath the Solfatara-Pisciarelli (Fig. 1a) and are in general of low
303 magnitude (maximum magnitude = 3.3) and of relatively shallow depths (Fig. 5a). The earthquakes'
304 occurrence rate manifestly increases since 2017-2018 (Fig. 5b). Note that Fig. 5b reports events
305 with magnitude ≥ 0.1 , for which the catalogue is reasonably complete in the observation period. The
306 absence of deep events at CFc (i.e. depth >3-4 km) likely reflects the high temperatures expected at
307 depth, and a very shallow brittle-ductile transition (3-5 km; Castaldo et al., 2019).

308

309 **3.4. Comparison of the different datasets**

310 A multivariate time-series analysis is attempted to compare the different observations. To this aim,
311 we compute the annual mean (annual number for the earthquakes) of each variable (red points in
312 Figs. 2, 3 and 5), focussing on the 2010-2020 period, for which most of the variables are available.
313 The approach based on the analysis of the annual values has the advantage of filtering out any
314 seasonally controlled variations. The multivariate analysis is not applied to the FCO₂-DDS (Fig.

315 3b) and to the CO₂ flux from Pisciarelli vents (Fig. 3c) because these measurements are sporadic
316 and not available for the entire period. In detail, a Principal Component Analysis (PCA) was
317 performed on the other FFR variables (air CO₂, FCO₂, RSAM) and earthquakes to simplify and
318 summarize the relationships among the multivariate set of data. We used the function *prcomp* of the
319 package *stats* of the R software (R Core Team, 2018), which performs PCA via a singular value
320 decomposition of the centered and scaled data matrix. This technique derives a new set of
321 uncorrelated variables (Principal Components, PC) using a linear combination of the original
322 variables, and ranks them in terms of their overall control on the variance. PCA is therefore used to
323 reduce the dimensionality of the data set, by choosing only those PCs that explain most of the
324 variance in the data. In practice, the PCA applied to the 4-variables matrix returns 4 PC, which
325 retain different proportions of the total variance: PC1 the 93.6%, PC2 the 3.9%, PC3 the 1.8%, and
326 PC4 the 0.7% (Table 1). The scores of these new variables are calculated multiplying the matrix of
327 the scaled original variables by the eigenvector matrix in Table 1 (namely, the eigenvectors of the
328 correlation matrix of the original data set). These results indicate that nearly the total (temporal)
329 variability of the data (~94%) is explained by PC1 only, which is defined by an almost identical
330 contribution of air CO₂, RSAM, FCO₂, and Earthquakes variables (see the coefficients of the first
331 eigenvector in Table 1).

332 This suggests that a single driving mechanism controls the variations of hydrothermal fluid flux and
333 earthquakes (Fig. 6), and as such summarizes well the temporal evolution of the hydrothermal part
334 of the CFC unrest. It is worth to note that PC1 is very well correlated with the P_{tot} and temperature,
335 estimated using the *vapour-liquid coexistence* model (Fig. 6). This supports our hypothesis that
336 increasing fluid pressure and temperature in the hydrothermal system is a causal factor in triggering
337 the CFC seismicity, and is the driver for the observed escalation in hydrothermal fluid release at the
338 surface.

339 In contrast, the *no-condensation* model outputs unrealistic results, as post-2015 estimated pressures
340 are unacceptably low (< atmospheric pressure, 1 bar) and decrease over the same temporal interval

341 during which earthquake occurrence rate and surface hydrothermal fluid fluxes are both visibly
342 increasing. This mismatch indicates that the assumption that fumarolic water concentrations are
343 currently fully representative of the deep, equilibrium compositions (Moretti et al., 2017) is
344 inconsistent with the observations.

345

346 **3.5. The conceptual model of the hydrothermal system and ‘hydrothermal’ seismicity**

347 The conceptual model based on the *vapour-liquid coexistence* assumption is sketched in Fig. 7a
348 over a 2-D resistivity model of Solfatara, derived by AMT (AudioMagnetoTelluric) measurements
349 (Siniscalchi et al., 2019). The section is dominated by a ~2 km long vertically elongated resistivity
350 structure in axis with Solfatara. This is the core of the hydrothermal system feeding the Solfatara-
351 Pisciarelli hydrothermal sites. It is interpreted as a permeable zone that favours gas ascent from the
352 hottest and deepest portions of the system. Hot, methane-free magmatic fluids enter the base (> 2
353 km depth) of the system, mix with and vaporize meteoric liquids, and ultimately create the
354 condition for CH₄ formation at temperatures > 360°C (Caliro et al., 2007). From that zone, a gas
355 plume rises up to 0.3-0.7 km where the resistive structure is interrupted by conductive layers (green,
356 cyan and blue colours) that reflect both hydrothermal altered zones and a liquid phase-dominated
357 environment (Siniscalchi et al., 2019). It is worth to note that, assuming a hydrostatic control on
358 fluid pressure, the inferred equilibration pressures of the *vapour-liquid coexistence* model (from 30
359 to 80 bar, considering both the DP and CV redox buffers, see section 3.1.2) correspond to gas
360 equilibration depths of 0.3-0.8 km, that coincide with the top of the resistive structure (Fig. 7). Here,
361 at the interface with the overlying clayed altered zones, the gas phase is expected to accumulate and
362 to reside for a sufficient time to allow the gas phase to re-equilibrate at the local T-P conditions.
363 From that zone, the gas moves toward the surface trough fractures, shallow gas pockets and liquid
364 bodies whose existence and complex geometry has been highlighted by detailed geo-electric
365 surveys (Byrdina et al., 2014; Gresse et al., 2017; Gresse et al., 2018).

366 According to (Chiodini et al., 2016), an escalating magmatic fluid inflow at the base of the
367 hydrothermal system causes its heating and pressurization, and in turn the increase of the CO₂
368 emission at the surface and seismicity (Fig. 6). A dense earthquake cluster is observed at 0.5-1 km
369 depth (Fig. 7b and c), and since this interval nicely corresponds to the gas equilibration depths
370 inferred above (0.3-0.8 m) is here interpreted as the head of the gas front feeding the hydrothermal
371 system. Thus, our inferred P_{tot} increase refers to such topmost portion of this seismogenetic vertical
372 gas plume. It is also noteworthy the existence of a second, deeper (>2 km) seismicity cluster that
373 corresponds to the source area irradiating the highest magnitude earthquakes (Fig. 7b): this structure
374 has been interpreted as the root of the gas plume, in which larger events are likely caused by pulsed
375 magmatic fluid injections (e.g., Giudicepietro et al., 2020).
376 Ultimately, the close spatial correspondence between the main seismogenetic volume (0.5-1 km)
377 and the gas equilibration zone (0.3-0.8 km) supports the idea that, similarly to the seismicity
378 induced by anthropogenic fluid injection, the generalised pressurization and heating of the CFC gas
379 dominated-hydrothermal system act as the main seismicity trigger (Fig. 7b and c).

380

381 **3.6. A mass balance of the steam associated with the CO₂ emission and hydrothermal** 382 **seismicity**

383 The observed escalation in surface gas release at Solfatara and Pisciarelli is an additional evident
384 sign for increased gas transport at depth, and of a generalised gas pressure build-up at source. Using
385 the numerous data of the CO₂ emission from the target area (FCO₂, Fig. 3a) we compute that the
386 total CO₂ emissions from Solfatara DDS increased from ~ 1000 t d⁻¹ in 2008-2010 up to 3000-4000
387 t d⁻¹ in 2019-2020 (Fig. 8). Considering that similar increments also affected the fumarolic vents
388 (Tamburello et al., 2019) we can roughly estimate the current total CO₂ emission from Solfatara-
389 Pisciarelli at ~ 5000 t d⁻¹. This flux ranks CFC among the first 8 top volcanic CO₂ emitters on Earth
390 (Fischer et al., 2019; Werner et al., 2019). Such an unusually large gas supply implies pressure-
391 build up in the gas source area (the hydrothermal system), and must inherently be associated with a

392 large thermal energy release (as steam and CO₂ are associated prior to condensation). We stress that
393 since gas pressurization is an exothermic process, it may itself be causing heating. In addition, the
394 pressurization of a steam-rich gas phase can induce its condensation, a process that at CFC
395 hydrothermal system is described by the *vapour-liquid coexistence* geochemical model.
396 Condensation can be shallow (forming the hot soils and mud pools that characterise the fumarolic
397 fields) or relatively deep. We attempt at establishing a steam mass balance for the hydrothermal
398 systems by dividing it into 3 components (Fig. 9a):

- 399 - the original steam emission at reservoir conditions (*reservoir emission* in Fig. 9a); this is
400 derived by multiplying the diffuse CO₂ flux (FCO₂-DDS) by the H₂O/CO₂ ratio in the gas
401 equilibration zone (derived from P_{H₂O} and P_{CO₂} estimates);
- 402 - the fraction of steam condensing in the sub-surface of the DDS (*DDS condensate* in Fig. 9a);
403 this computed by multiplying FCO₂-DDS by the fumarolic H₂O/CO₂;
- 404 - the fraction of steam that condense at depth (*deep condensate* in Fig. 9a, b and c); given by the
405 difference *reservoir emission - DDS condensate*.

406 It is worth to note that the inferred temporal evolution of the *deep condensate* mass match nicely
407 that of ‘hydrothermal’ seismicity (Fig. 9b and c), i.e. of the events occurred in the volume
408 containing the hydrothermal system (see Fig. 7b and c). In our interpretation, the *deep condensate*
409 represents the fraction of the original steam/thermal energy budget that can potentially trigger
410 earthquakes because the condensed liquid can lubricate pre-existing fractures and because
411 hydrothermal host rocks get hotter, increase in volume by thermal dilatation, and finally fracture as
412 they reach a failure threshold. The total thermal energy involved in *deep condensation* from 2004 to
413 2020 is $\sim 4 \times 10^{14}$ J (computed from the latent heat of condensation), and is thus well enough to
414 justify the observed seismicity (being 5 orders of magnitude higher than the cumulative energy of
415 all the CFC earthquakes, $\sim 1.5 \times 10^9$ J, [http://www.ov.ingv.it/ov/bollettini-mensili-](http://www.ov.ingv.it/ov/bollettini-mensili-campania/Bollettino_Mensile_Campi_Flegrei_2020_10.pdf)
416 [campania/Bollettino_Mensile_Campi_Flegrei_2020_10.pdf](http://www.ov.ingv.it/ov/bollettini-mensili-campania/Bollettino_Mensile_Campi_Flegrei_2020_10.pdf)).

417

418 **4. Conclusions**

419 We use a novel multidisciplinary approach to characterise the spatial-temporal evolution of the
420 hydrothermal unrest currently affecting CFc. A multivariate analysis shows that different datasets,
421 including a set of fluid flow-related variables and earthquake occurrence, share a common evolution
422 during 2010-2020, and are fully described by a single component that explains 94% of their total
423 variance. This component, whose values exhibit a sharp increase from 2018 onward, is well
424 correlated with escalating pressure and temperature of the hydrothermal system inferred from
425 geochemical modelling of fumarole composition. The P-T increase occurs in a gas-dominated zone,
426 located at depths of < 1 km below the main hydrothermal sites, which corresponds to the main
427 cluster of low magnitude, post 2004 earthquakes. This temporal and spatial association between
428 hydrothermal P-T and seismicity brings compelling evidence for the role played by pressurising
429 hydrothermal fluids in driving volcano seismicity at CFc. Our results bring evidence for the
430 seismogenetic role played by magmatic gas injection into hydrothermal systems, and are thus of
431 general relevance for other volcanoes in similar contexts.

432

433 **Acknowledgments:**

434 We would like to remember the researchers Roberto Cioni and Egizio Corazza who recently passed
435 away: they began to sample and analyze Solfatara fumaroles in early 1980's, starting the Solfatara
436 fumaroles database.

437 **Funding:** This work was supported by MIUR, project n. PRIN2017-2017LMNLAW
438 "Connect4Carbon".

439

440

441 **References**

442 Aiuppa, A., Fiorani, L., Santoro, S., Parracino, S., Nuvoli, M., Chiodini, G., Minopoli, C. and
443 Tamburello, G., 2015. New ground-based lidar enables volcanic CO₂ flux measurements.
444 Sci. Rep., 5. <https://doi.org/10.1038/srep13614>.

445 Aiuppa, A., Tamburello, G., Di Napoli, R., Cardellini, C., Chiodini, G., Giudice, G., Grassa, F. and
446 Pedone, M., 2013. First observations of the fumarolic gas output from a restless caldera:
447 Implications for the current period of unrest (2005-2013) at Campi Flegrei. *Geochem.*
448 *Geophys. Geosys.*, 14(10), 4153-4169. <https://doi.org/10.1002/ggge.20261>.

449 Amoruso, A., Crescentini, L. and Sabetta, I., 2014a. Paired deformation sources of the Campi
450 Flegrei caldera (Italy) required by recent (1980–2010) deformation history. *J. Geophys.*
451 *Res.*, 119(2), 858-879. <https://doi.org/10.1002/2013JB010392>.

452 Amoruso, A., Crescentini, L., Sabetta, I., De Martino, P., Obrizzo, F. and Tammaro, U., 2014b.
453 Clues to the cause of the 2011–2013 Campi Flegrei caldera unrest, Italy, from continuous
454 GPS data. *Geophys. Res. Lett.*, 41, 3081-3088. <https://doi.org/10.1002/2014GL059539>.

455 Bianco, F., Del Pezzo, E., Saccorotti, G. and Ventura, G., 2004. The role of hydrothermal fluids in
456 triggering the July–August 2000 seismic swarm at Campi Flegrei, Italy: evidence from
457 seismological and mesostructural data. *J. Volcanol. Geother. Res.*, 133(1), 229-246.
458 [https://doi.org/10.1016/S0377-0273\(03\)00400-1](https://doi.org/10.1016/S0377-0273(03)00400-1).

459 Bruno, P.P.G., Ricciardi, G.P., Petrillo, Z., Di Fiore, V., Troiano, A. and Chiodini, G., 2007.
460 Geophysical and hydrogeological experiments from a shallow hydrothermal system at
461 Solfatara Volcano, Campi Flegrei, Italy: Response to caldera unrest. *J. Geophys. Res.*,
462 112(B6). <https://doi.org/10.1029/2006JB004383>.

463 Byrdina, S., Vandemeulebrouck, J., Cardellini, C., Legaz, A., Camerlynck, C., Chiodini, G.,
464 Lebourg, T., Gresse, M., Bascou, P., Motos, G., Carrier, A. and Caliro, S., 2014. Relations
465 between electrical resistivity, carbon dioxide flux, and self-potential in the shallow
466 hydrothermal system of Solfatara (Phlegrean Fields, Italy). *J. Volcanol. Geother. Res.*, 283,
467 172-182. <https://doi.org/10.1016/j.jvolgeores.2014.07.010>.

468 Caliro, S., Chiodini, G., Moretti, R., Avino, R., Granieri, D., Russo, M. and Fiebig, J., 2007. The
469 origin of the fumaroles of La Solfatara (Campi Flegrei, South Italy). *Geochim. Cosmochim.*
470 *Acta*, 71(12), 3040-3055. <https://doi.org/10.1016/j.gca.2007.04.007>.

471 Caliro, S., Chiodini, G. and Paonita, A., 2014. Geochemical evidences of magma dynamics at
472 Campi Flegrei (Italy). *Geochim. Cosmochim. Acta*, 132, 1-15.
473 <https://doi.org/10.1016/j.gca.2014.01.021>.

474 Cardellini, C., Chiodini, G. and Frondini, F., 2003. Application of stochastic simulation to CO₂ flux
475 from soil: Mapping and quantification of gas release. *J. Geophys. Res.*, 108(B9).
476 <https://doi.org/10.1029/2002JB002165>.

477 Cardellini, C., Chiodini, G., Frondini, F., Avino, R., Bagnato, E., Caliro, S., Lelli, M. and Rosiello,
478 A., 2017. Monitoring diffuse volcanic degassing during volcanic unrests: The case of Campi

479 Flegrei (Italy). *Sci. Rep.*, 7(1). <https://doi.org/10.1038/s41598-017-06941-2>.

480 Castaldo, R., D'Auria, L., Pepe, S., Solaro, G., De Novellis, V. and Tizzani, P., 2019. The impact of
481 crustal rheology on natural seismicity: Campi Flegrei caldera case study. *Geosc. Front.*,
482 10(2), 453-466. <https://doi.org/10.1016/j.gsf.2018.02.003>.

483 Chiodini, G. and Marini, L., 1998. Hydrothermal gas equilibria: The H₂O-H₂-CO₂-CO-CH₄ system.
484 *Geochim. Cosmochim. Acta*, 62(15), 2673-2687. [https://doi.org/10.1016/S0016-](https://doi.org/10.1016/S0016-7037(98)00181-1)
485 7037(98)00181-1.

486 Chiodini, G., Cioni, R., Magro, G., Marini, L., Panichi, C., Raco, B. and Russo, M., 1996. Chemical
487 and isotopic variations of Bocca Grande fumarole (Solfatara Volcano, Phlegrean Fields).
488 *Acta Vulcanol.*, 8, 129-138.

489 Chiodini, G., Cioni, R., Guidi, M., Raco, B. and Marini, L., 1998. Soil CO₂ flux measurements in
490 volcanic and geothermal areas. *App. Geochem.*, 13(5), 543-552.
491 [https://doi.org/10.1016/S0883-2927\(97\)00076-0](https://doi.org/10.1016/S0883-2927(97)00076-0).

492 Chiodini, G., Frondini, F., Cardellini, C., Granieri, D., Marini, L. and Ventura, G., 2001. CO₂
493 degassing and energy release at Solfatara volcano, Campi Flegrei, Italy. *J. Geophys. Res.*,
494 106(B8), 16213-16221. <https://doi.org/10.1029/2001JB000246>.

495 Chiodini, G., Vandemeulebrouck, J., Caliro, S., D'Auria, L., De Martino, P., Mangiacapra, A. and
496 Petrillo, Z., 2015. Evidence of thermal-driven processes triggering the 2005-2014 unrest at
497 Campi Flegrei caldera. *Earth Planet. Sci. Lett.*, 414, 58-67.
498 <https://doi.org/10.1016/j.epsl.2015.01.012>.

499 Chiodini, G., Paonita, A., Aiuppa, A., Costa, A., Caliro, S., De Martino, P., Acocella, V. and
500 Vandemeulebrouck, J., 2016. Magmas near the critical degassing pressure drive volcanic
501 unrest towards a critical state. *Nat. Comm.*, 7. <https://doi.org/10.1038/ncomms13712>.

502 Chiodini, G., Selva, J., Del Pezzo, E., Marsan, D., De Siena, L., D'Auria, L., Bianco, F., Caliro, S.,
503 De Martino, P., Ricciolino, P. and Petrillo, Z., 2017a. Clues on the origin of post-2000
504 earthquakes at Campi Flegrei caldera (Italy). *Sci. Rep.*, 7(1). [https://doi.org/10.1038/s41598-](https://doi.org/10.1038/s41598-017-04845-9)
505 017-04845-9.

506 Chiodini, G., Giudicepietro, F., Vandemeulebrouck, J., Aiuppa, A., Caliro, S., De Cesare, W.,
507 Tamburello, G., Avino, R., Orazi, M. and D'Auria, L., 2017b. Fumarolic tremor and
508 geochemical signals during a volcanic unrest. *Geology*, 45(12), 1131-1134.
509 <https://doi.org/10.1130/G39447.1>.

510 Chiodini, G., Cardellini, C., Di Luccio, F., Selva, J., Frondini, F., Caliro, S., Rosiello, A., Beddini,
511 G. and Ventura, G., 2020. Correlation between tectonic CO₂ Earth degassing and seismicity
512 is revealed by a 10-year record in the Apennines, Italy. *Sci. Advanc.*, 6(35), eabc2938.

513 <https://doi.org/10.1126/sciadv.abc2938>.

514 Cioni, R. and Corazza, E., 1981. Medium-temperature fumarolic gas sampling. *Bull. Volcanol.*,
515 44(1), 23-29. <https://doi.org/10.1007/BF02598186>.

516 Cioni, R., Corazza, E. and Marini, L., 1984. The gas/steam ratio as indicator of heat transfer at the
517 Solfatara fumaroles, Phlegraean Fields (Italy). *Bull. Volcanol.*, 47, 295-302.
518 <https://doi.org/10.1007/BF01961560>.

519 Costa, A., Folch, A., Macedonio, G., Giaccio, B., Isaia, R. and Smith, V.C., 2012. Quantifying
520 volcanic ash dispersal and impact of the Campanian Ignimbrite super-eruption. *Geophys.*
521 *Res. Lett.*, 39(10). <https://doi.org/10.1029/2012GL051605>.

522 D'Amore, F. and Panichi, C., 1980. Evaluation of deep temperatures of hydrothermal systems by a
523 new gas geothermometer. *Geochim. Cosmochim. Acta*, 44(3), 549-556.
524 [https://doi.org/10.1016/0016-7037\(80\)90051-4](https://doi.org/10.1016/0016-7037(80)90051-4).

525 D'Auria, L., Giudicepietro, F., Aquino, I., Borriello, G., Del Gaudio, C., Lo Bascio, D., Martini, M.,
526 Ricciardi, G.P., Ricciolino, P. and Ricco, C., 2011. Repeated fluid-transfer episodes as a
527 mechanism for the recent dynamics of Campi Flegrei caldera (1989–2010). *J. Geophys.*
528 *Res.*, 116(B4). <https://doi.org/10.1029/2010JB007837>.

529 Del Gaudio, C., Aquino, I., Ricciardi, G.P., Ricco, C. and Scandone, R., 2010. Unrest episodes at
530 Campi Flegrei: A reconstruction of vertical ground movements during 1905–2009. *J.*
531 *Volcanol. Geother. Res.*, 195(1), 48-56. <https://doi.org/10.1016/j.jvolgeores.2010.05.014>.

532 Deutsch, C.V. and Journel, A.G., 1998. *GSLIB: Geostatistical Software Library and Users Guide*.
533 Oxford University Press, Oxford, New York 369 pp.

534 Ellsworth, W.L., 2013. Injection-Induced Earthquakes. *Science*, 341(6142), 1225942.
535 <https://doi.org/10.1126/science.1225942>.

536 Endo, E.T. and Murray, T., 1991. Real-time Seismic Amplitude Measurement (RSAM): a volcano
537 monitoring and prediction tool. *Bull. Volcanol.*, 53(7), 533-545.
538 <https://doi.org/10.1007/BF00298154>.

539 Farrar, C.D., Sorey, M.L., Evans, W.C., Howle, J.F., Kerr, B.D., Kennedy, B.M., King, C.Y. and
540 Southon, J.R., 1995. Forest-killing diffuse CO₂ emission at Mammoth Mountain as a sign of
541 magmatic unrest. *Nature*, 376(6542), 675-678. <https://doi.org/10.1038/376675a0>.

542 Fischer, T., Matyska, C. and Heinicke, J., 2017. Earthquake-enhanced permeability – evidence from
543 carbon dioxide release following the ML 3.5 earthquake in West Bohemia. *Earth Planet. Sci.*
544 *Lett.*, 460, 60-67. <https://doi.org/10.1016/j.epsl.2016.12.001>.

545 Fischer, T.P., Arellano, S., Carn, S., Aiuppa, A., Galle, B., Allard, P., Lopez, T., Shinohara, H.,
546 Kelly, P., Werner, C., Cardellini, C. and Chiodini, G., 2019. The emissions of CO₂ and other

547 volatiles from the world's subaerial volcanoes. *Sci. Rep.*, 9(1), 18716.
548 <https://doi.org/10.1038/s41598-019-54682-1>.

549 Giggenbach, W.F., 1980. Geothermal gas equilibria. *Geochim. Cosmochim. Acta*, 44, 2021-2032.
550 [https://doi.org/10.1016/0016-7037\(80\)90200-8](https://doi.org/10.1016/0016-7037(80)90200-8).

551 Giggenbach, W.F., 1987. Redox processes governing the chemistry of fumarolic gas discharges
552 from White Island, New Zealand. *Appl. Geochem.*, 2(2), 143-161.
553 [https://doi.org/10.1016/0883-2927\(87\)90030-8](https://doi.org/10.1016/0883-2927(87)90030-8).

554 Girault, F., Adhikari, L.B., France-Lanord, C., Agrinier, P., Koirala, B.P., Bhattarai, M., Mahat,
555 S.S., Groppo, C., Rolfo, F., Bollinger, L. and Perrier, F., 2018. Persistent CO₂ emissions
556 and hydrothermal unrest following the 2015 earthquake in Nepal. *Nat. Commun.*, 9(1),
557 2956. <https://doi.org/10.1038/s41467-018-05138-z>.

558 Giudicepietro, F., Chiodini, G., Avino, R., Brandi, G., Caliro, S., De Cesare, W., Galluzzo, D.,
559 Esposito, A., La Rocca, A., Lo Bascio, D., Obrizzo, F., Pinto, S., Ricci, T., Ricciolino, P.,
560 Siniscalchi, A., Tramelli, A., Vandemeulebrouck, J. and Macedonio, G., 2020. Tracking
561 episodes of seismicity and gas transport in Campi Flegrei caldera trough seismic,
562 geophysical and geochemical measurements. *Seismol. Res. Lett.* , in press, 1-11.
563 <https://doi.org/10.1785/0220200223>.

564 Giudicepietro, F., Chiodini, G., Caliro, S., De Cesare, W., Esposito, A.M., Galluzzo, D., Lo Bascio,
565 D., Macedonio, G., Orazi, M., Ricciolino, P. and Vandemeulebrouck, J., 2019. Insight Into
566 Campi Flegrei Caldera Unrest Through Seismic Tremor Measurements at Pisciarelli
567 Fumarolic Field. *Geochem. Geophys. Geosys.*, 20(11), 5544-5555.
568 <https://doi.org/10.1029/2019GC008610>.

569 Granieri, D., Avino, R. and Chiodini, G., 2009. Carbon dioxide diffuse emission from the soil: ten
570 years of observations at Vesuvio and Campi Flegrei (Pozzuoli), and linkages with volcanic
571 activity. *Bull. Volcanol.*, 72(1), 103. <https://doi.org/10.1007/s00445-009-0304-8>.

572 Gresse, M., Vandemeulebrouck, J., Byrdina, S., Chiodini, G., Revil, A., Johnson, T.C., Ricci, T.,
573 Vilardo, G., Mangiacapra, A., Lebourg, T., Grangeon, J., Bascou, P. and Metral, L., 2017.
574 Three-Dimensional Electrical Resistivity Tomography of the Solfatara Crater (Italy):
575 Implication for the Multiphase Flow Structure of the Shallow Hydrothermal System. *J.*
576 *Geophys. Res.*, 122(11), 8749-8768. <https://doi.org/10.1002/2017JB014389>.

577 Gresse, M., Vandemeulebrouck, J., Byrdina, S., Chiodini, G., Roux, P., Rinaldi, A.P., Wathelet, M.,
578 Ricci, T., Letort, J., Petrillo, Z., Tuccimei, P., Lucchetti, C. and Sciarra, A., 2018. Anatomy
579 of a fumarolic system inferred from a multiphysics approach. *Sci. Rep.*, 8(1), 7580.
580 <https://doi.org/10.1038/s41598-018-25448-y>.

581 Hotovec-Ellis, A.J., Shelly, D.R., Hill, D.P., Pitt, A.M., Dawson, P.B. and Chouet, B.A., 2018.
582 Deep fluid pathways beneath Mammoth Mountain, California, illuminated by migrating
583 earthquake swarms. *Sci. Advanc.*, 4(8), eaat5258. <https://doi.org/10.1126/sciadv.aat5258>.

584 Hubbert, M. and Rubey, W., 1959. Role of fluid pressure in mechanics of overthrust faulting. *Geol.*
585 *Soc. Am.*, 70, 115-166.

586 Keranen, K.M. and Weingarten, M., 2018. Induced Seismicity. *Ann. Rev. Earth Planet. Sci.*, 46(1),
587 149-174. <https://doi.org/10.1146/annurev-earth-082517-010054>.

588 Kilburn, C.R.J., De Natale, G. and Carlino, S., 2017. Progressive approach to eruption at Campi
589 Flegrei caldera in southern Italy. *Nat. Comm.*, 8(1), 15312.
590 <https://doi.org/10.1038/ncomms15312>.

591 Lewicki, J.L., Hilley, G.E., Shelly, D.R., King, J.C., McGeehin, J.P., Mangan, M. and Evans, W.C.,
592 2014. Crustal migration of CO₂-rich magmatic fluids recorded by tree-ring radiocarbon and
593 seismicity at Mammoth Mountain, CA, USA. *Earth Planet. Sci. Lett.*, 390, 52-58.
594 <https://doi.org/10.1016/j.epsl.2013.12.035>.

595 Miller, S.A., 2013. The Role of Fluids in Tectonic and Earthquake Processes. In: R. Dmowska
596 (Editor), *Advanc. Geophys. Advances in Geophysics*, pp. 1-46.
597 <https://doi.org/10.1016/b978-0-12-380940-7.00001-9>.

598 Moretti, R., De Natale, G. and Troise, C., 2017. A geochemical and geophysical reappraisal to the
599 significance of the recent unrest at Campi Flegrei caldera (Southern Italy). *Geochem.*
600 *Geophys. Geosys.*, 18(3), 1244-1269 <https://doi.org/10.1002/2016GC006569>.

601 Orsi, G., Civetta, L., Del Gaudio, C., de Vita, S., Di Vito, M.A., Isaia, R., Petrazzuoli, S.M.,
602 Ricciardi, G.P. and Ricco, C., 1999. Short-term ground deformations and seismicity in the
603 resurgent Campi Flegrei caldera (Italy): an example of active block-resurgence in a densely
604 populated area. *J. Volcanol. Geother. Res.*, 91(2), 415-451. [https://doi.org/10.1016/S0377-](https://doi.org/10.1016/S0377-0273(99)00050-5)
605 [0273\(99\)00050-5](https://doi.org/10.1016/S0377-0273(99)00050-5).

606 Pedone, M., Aiuppa, A., Giudice, G., Grassa, F., Cardellini, C., Chiodini, G. and Valenza, M.,
607 2014. Volcanic CO₂ flux measurement at Campi Flegrei by tunable diode laser absorption
608 spectroscopy. *Bull. Volcanol.*, 76(4). <https://doi.org/10.1007/s00445-014-0812-z>.

609 Pfeiffer, L., Wanner, C. and Lewicki, J.L., 2018. Unraveling the dynamics of magmatic CO₂
610 degassing at Mammoth Mountain, California. *Earth Planet. Sci. Lett.*, 484, 318-328.
611 <https://doi.org/10.1016/j.epsl.2017.12.038>.

612 Queißer, M., Granieri, D., Burton, M., Arzilli, F., Avino, R. and Carandente, A., 2017. Increasing
613 CO₂ flux at Pisciarelli, Campi Flegrei, Italy. *Solid Earth*, 8(5), 1017-1024.
614 <https://doi.org/10.5194/se-8-1017-2017>.

615 R Core Team, 2018. R: A language and environment for statistical computing. R Foundation for
616 Statistical Computing, Vienna, Austria.

617 Saccorotti, G., Petrosino, S., Bianco, F., Castellano, M., Galluzzo, D., La Rocca, M., Del Pezzo, E.,
618 Zaccarelli, L. and Cusano, P., 2007. Seismicity associated with the 2004–2006 renewed
619 ground uplift at Campi Flegrei Caldera, Italy. *Phys. Earth Planet. Inter.*, 165(1), 14-24.
620 <https://doi.org/10.1016/j.pepi.2007.07.006>.

621 Selva, J., Marzocchi, W., Papale, P. and Sandri, L., 2012. Operational eruption forecasting at high-
622 risk volcanoes: the case of Campi Flegrei, Naples. *J. App. Volcanol.*, 1(1), 5.
623 <https://doi.org/10.1186/2191-5040-1-5>.

624 Sibson, R.H., 1992. Implications of fault-valve behaviour for rupture nucleation and recurrence.
625 *Tectonophysics* 211, 283-293. [https://doi.org/10.1016/0040-1951\(92\)90065-E](https://doi.org/10.1016/0040-1951(92)90065-E).

626 Siniscalchi, A., Tripaldi, S., Romano, G., Chiodini, G., Improta, L., Petrillo, Z., D'Auria, L., Caliro,
627 S. and Avino, R., 2019. Reservoir Structure and Hydraulic Properties of the Campi Flegrei
628 Geothermal System Inferred by Audiomagnetotelluric, Geochemical, and Seismicity Study.
629 *J. Geophys. Res.*, 124(6), 5336-5356. <https://doi.org/10.1029/2018JB016514>.

630 Smith, V.C., Isaia, R. and Pearce, N.J.G., 2011. Tephrostratigraphy and glass compositions of post-
631 15 kyr Campi Flegrei eruptions: implications for eruption history and chronostratigraphic
632 markers. *Quatern. Sci. Rev.*, 30(25), 3638-3660.
633 <https://doi.org/10.1016/j.quascirev.2011.07.012>.

634 Sorey, M.L., Evans, W.C., Kennedy, B.M., Farrar, C.D., Hainsworth, L.J. and Hausback, B., 1998.
635 Carbon dioxide and helium emissions from a reservoir of magmatic gas beneath Mammoth
636 Mountain, California. *J. Geophys. Res.*, 103(7), 15303-15323.
637 <https://doi.org/10.1029/98JB01389>.

638 Stull, D.R., Westrum, E.F. and Sinke, G.G., 1969. The chemical thermodynamics of organic
639 compounds. Wiley, New York, 865 pp.

640 Tamburello, G., Caliro, S., Chiodini, G., De Martino, P., Avino, R., Minopoli, C., Carandente, A.,
641 Rouwet, D., Aiuppa, A., Costa, A., Bitetto, M., Giudice, G., Francofonte, V., Ricci, T.,
642 Sciarra, A., Bagnato, E. and Capecchiacci, F., 2019. Escalating CO₂ degassing at the
643 Pisciarelli fumarolic system, and implications for the ongoing Campi Flegrei unrest. *J.*
644 *Volcanol. Geother. Res.*, 384, 151-157. <https://doi.org/10.1016/j.jvolgeores.2019.07.005>.

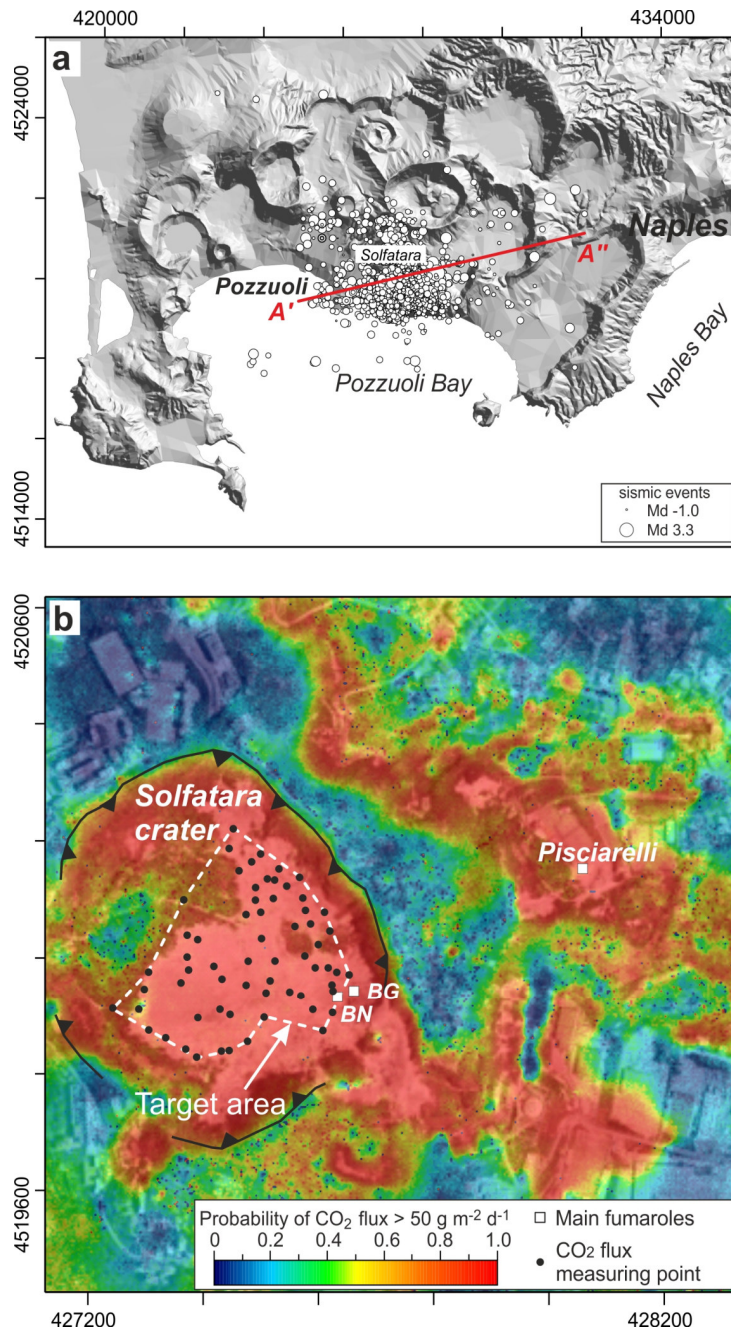
645 Werner, C., Bergfeld, D., Farrar, C.D., Doukas, M.P., Kelly, P.J. and Kern, C., 2014. Decadal-scale
646 variability of diffuse CO₂ emissions and seismicity revealed from long-term monitoring
647 (1995–2013) at Mammoth Mountain, California, USA. *J. Volcanol. Geother. Res.*, 289, 51-
648 63. <https://doi.org/10.1016/j.jvolgeores.2014.10.020>.

649 Werner, C., Fischer, T.P., Aiuppa, A., Edmonds, M., Cardellini, C., Carn, S., Chiodini, G., Cottrell,
 650 E., Burton, M., Shinohara, H. and Allard, P., 2019. Carbon Dioxide Emissions from
 651 Subaerial Volcanic Regions: Two Decades in Review. In: B.N. Orcutt, I. Daniel and R.
 652 Dasgupta (Eds.), Deep Carbon: Past to Present. Cambridge University Press, Cambridge, pp.
 653 188-236. <https://doi.org/10.1017/9781108677950>.

656 **Table 1.** Principal Component Analysis (PCA). Results of the PCA applied to the variables FCO₂,
 657 RSAM, air CO₂ and earthquakes.

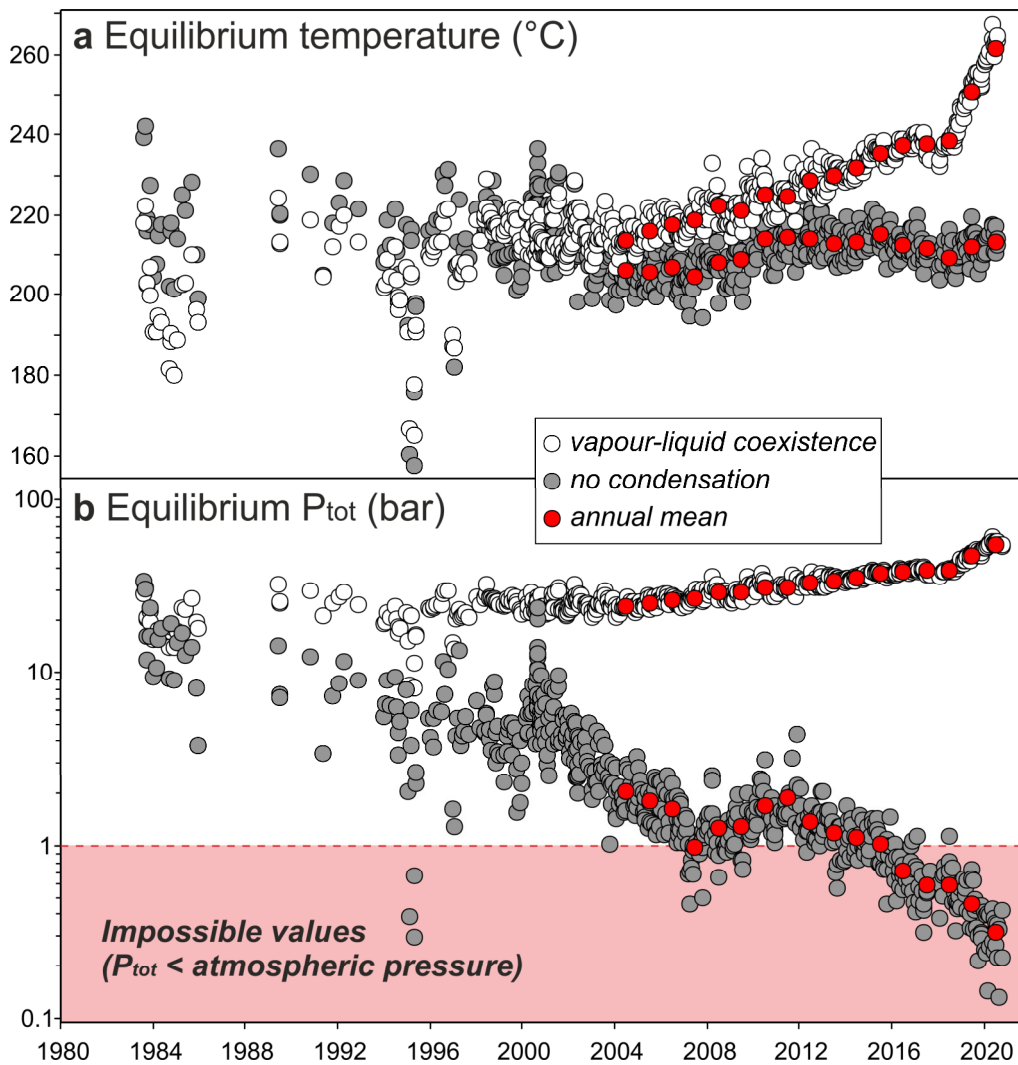
Variables	Eigenvectors			
	PC1	PC2	PC3	PC4
FCO ₂	0.4993	0.3342	-0.7991	0.0215
RSAM	0.5100	-0.0659	0.2692	-0.8143
air CO ₂	0.4914	-0.7896	-0.0134	0.3672
earthquakes	0.4992	0.5103	0.5373	0.4491
Importance of components	PC1	PC2	PC3	PC4
Variance	3.7591	0.1430	0.0736	0.0243
Proportion of variance	0.9398	0.0357	0.0184	0.0061
Cumulative proportion	0.9398	0.9755	0.9939	1.0000

658
 659
 660



661

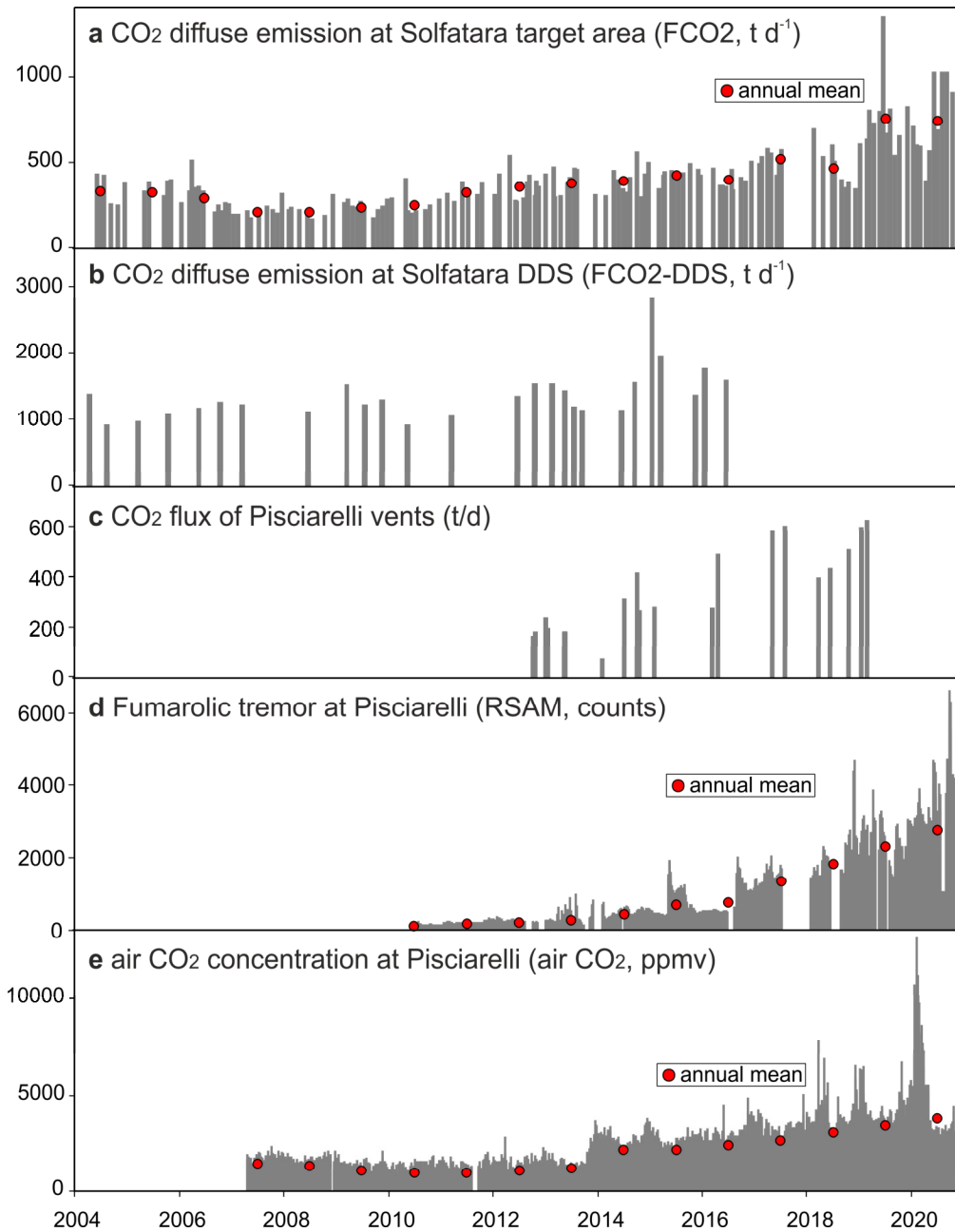
662 **Fig. 1.** Location map. a) Campi Flegrei caldera and location of the 2004-2020 earthquakes. The A'-
 663 A'' line refers to the vertical section reported in Fig. 6. b) Map of the Solfatara diffuse degassing
 664 structure (DDS) showing the locations of the target area, the monitored 63 points and the main
 665 fumaroles. The map, based on 13,158 CO₂ flux measurements from 1998 to 2016 (Cardellini et al.,
 666 2017), illustrates the probability that the simulated CO₂ flux is greater than 50 g m⁻² d⁻¹, selected as
 667 the threshold for a pure biogenic CO₂ flux. Coordinates are expressed in UTM-WGS84



668

669 **Fig. 2.** T-P estimates. a) Equilibrium temperatures and b) pressures estimated with two alternative

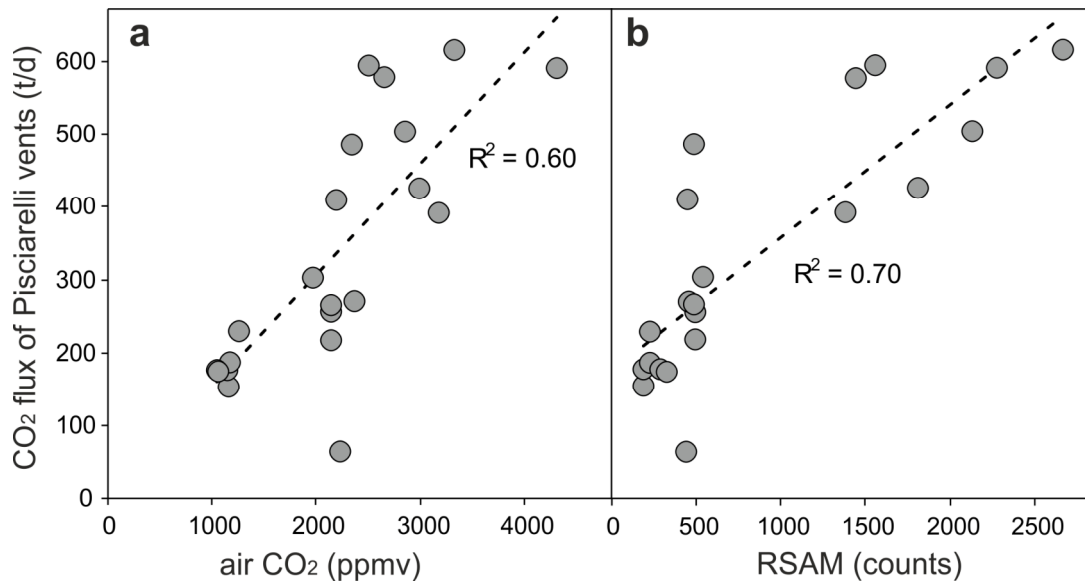
670 geochemical models (see the text) from the 1983-2020 compositions of BG and BN fumaroles.



671

672

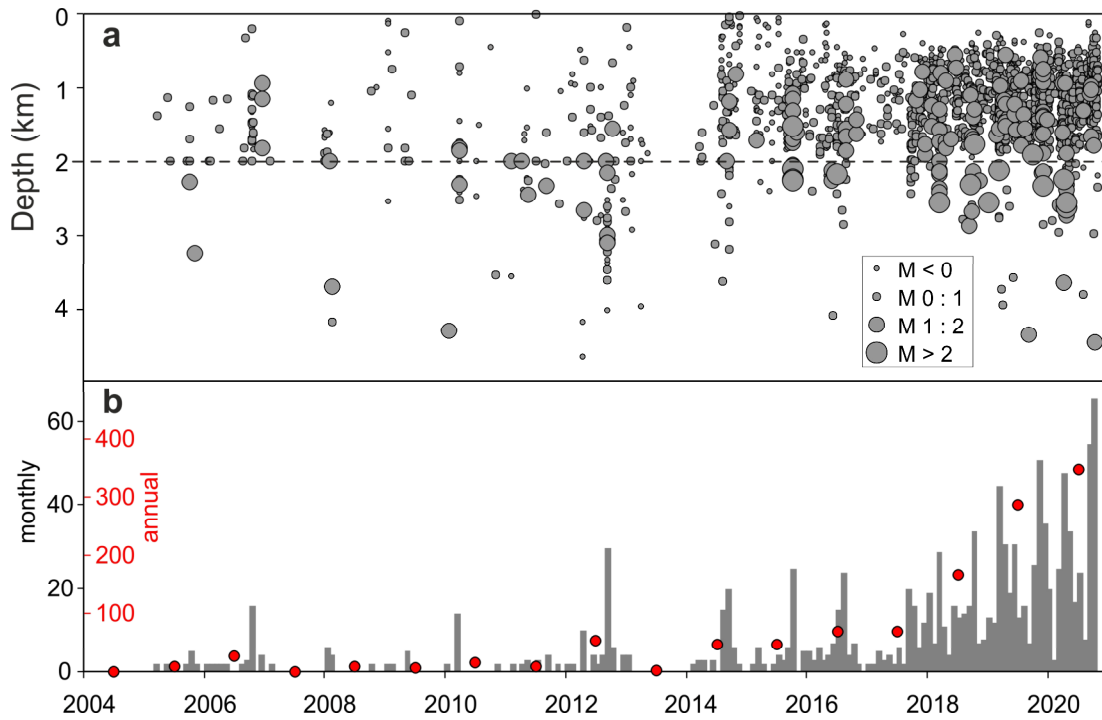
Fig. 3. Chronograms of the FFR variables. Annual means are reported with red symbols.



673

674

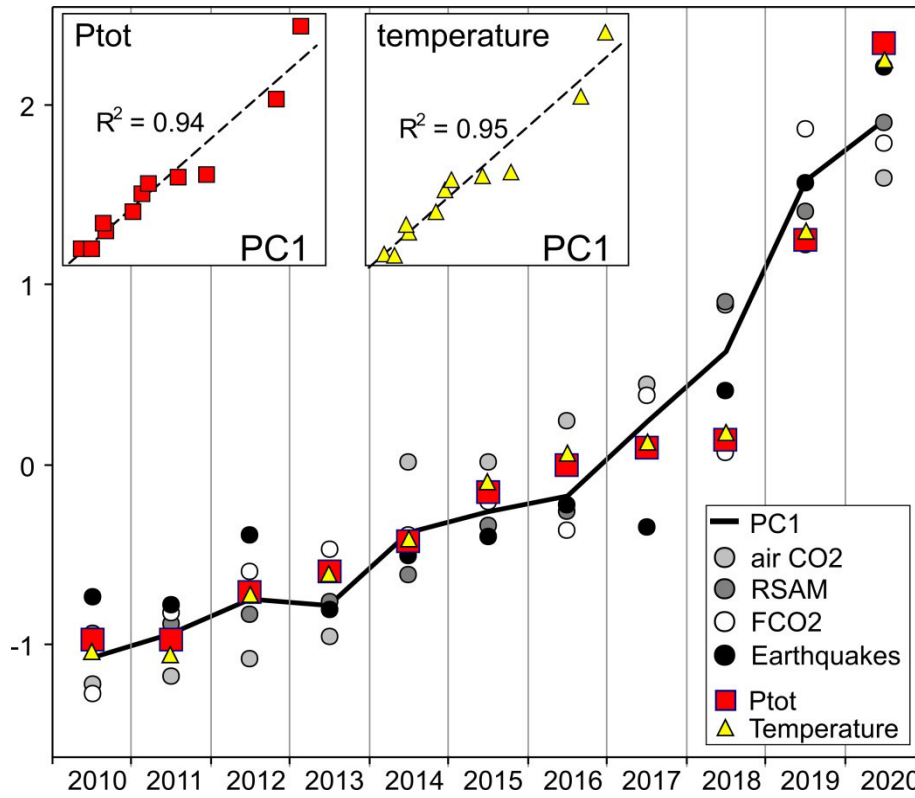
675 **Fig. 4.** air CO₂ and RSAM vs CO₂ flux of Pisciarelli vents. RSAM and air CO₂ are reported as the
 676 mean values measured at the time of the CO₂ flux campaign ± 30 days.



677

678

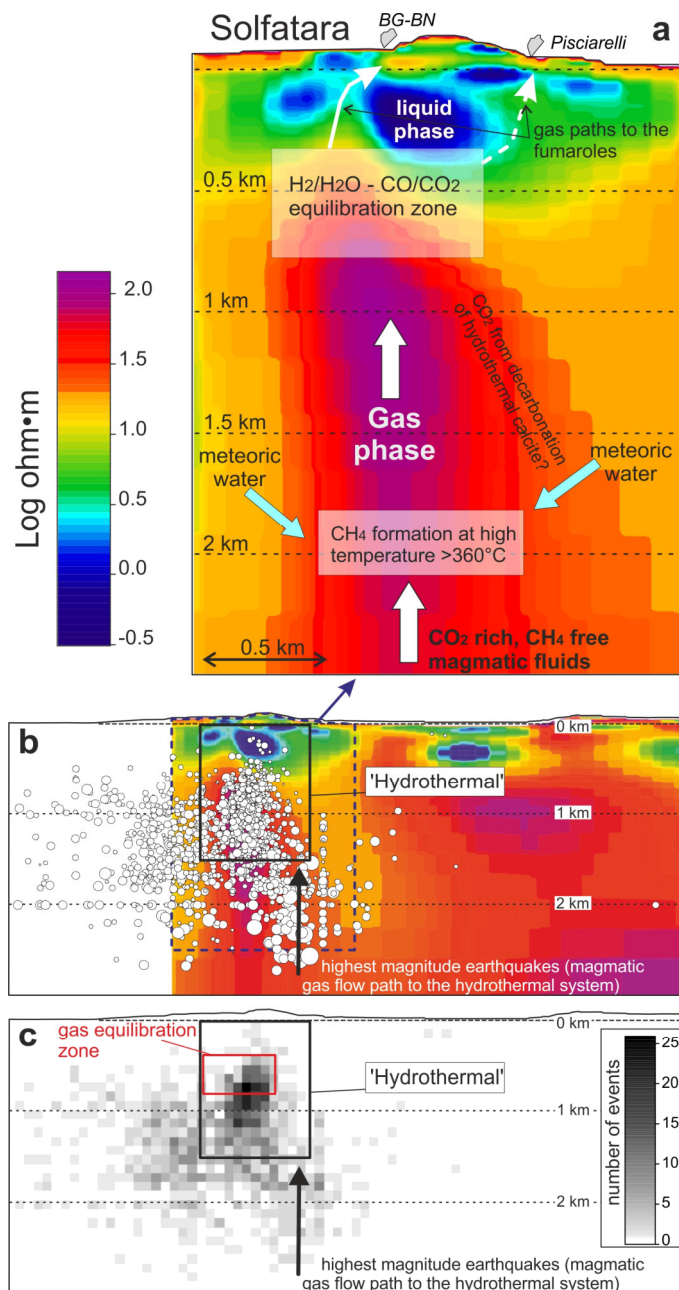
679 **Fig. 5.** CFc earthquakes from 2004 to October 2020. a) chronogram of depths and magnitudes; b)
 680 monthly (gray histogram) and annual (red symbols) number of earthquakes with Magnitude > 0.1 ;
 681 the 2020 annual number of earthquakes has been scaled over the entire year.



682

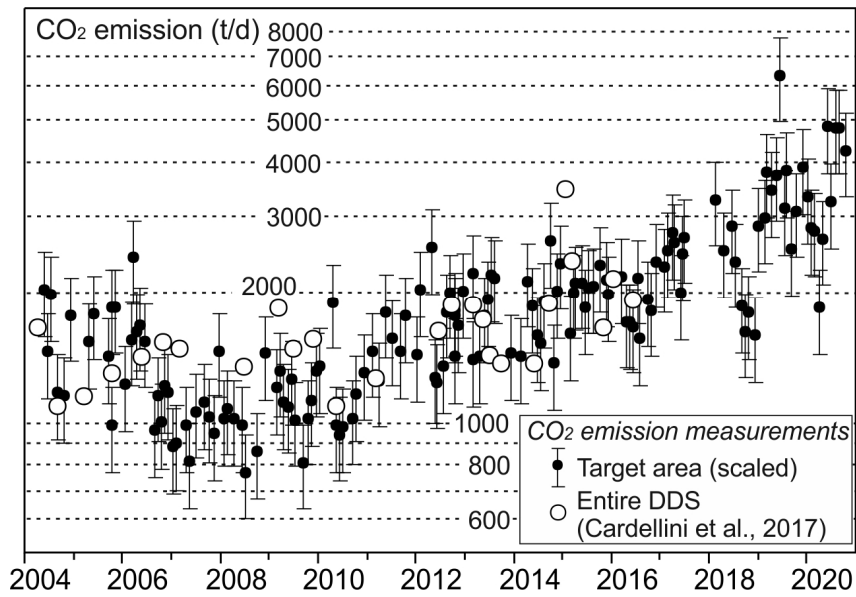
683

684 **Fig. 6.** Results of the PCA and Ptot. Chronograms of the z-scores of the FFR variables (air CO₂,
 685 RSAM, FCO₂), earthquakes occurrence, PC1, and the Ptot-temperature estimations based on the
 686 *vapour-liquid coexistence model* (all the variables are reported as annual means; the z-score is equal
 687 to the variable minus the mean divided for the standard deviation). The FFR variables and the
 688 Earthquakes occurrence were analysed with a PCA and PC1 is the resulting main component
 689 explaining their 94% total variance. PC1 is plotted against Ptot and temperature in the insets.



690

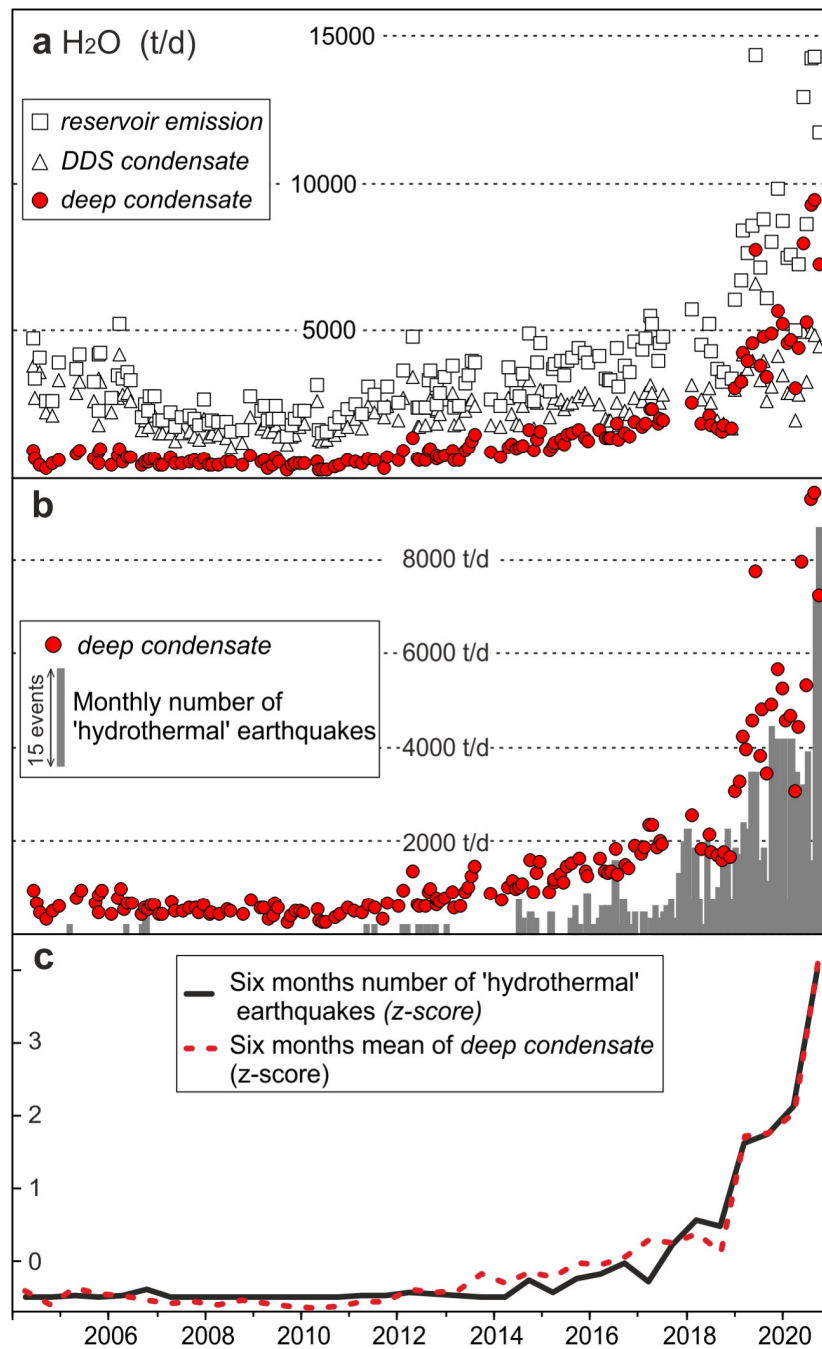
691 **Fig. 7.** Conceptual model and seismicity. a) Geochemical conceptual model of the hydrothermal
 692 system feeding the Solfatara-Pisciarelli manifestations sketched over a resistivity section (redraw
 693 from Siniscalchi et al. (2019)). b) section (A'-A'' in Fig. 1A) showing the relations between
 694 earthquake location (distance < 0.6 km from the section) and resistivity. The dimension of the white
 695 circles is proportional to the magnitude of the events. c) 2 D density map of earthquakes in the A'-
 696 A'' section (computed as the number of events projected on cells of 100×100 m²). The
 697 'hydrothermal' box is a section of a parallelepiped of 1.2×1.2×1.5 km assumed to contain the
 698 hydrothermal system (see the text and Fig. 9).



699

700

701 **Fig. 8.** CO₂ emission from diffuse degassing at Solfatara DDS during 2004-2020 The black dots
 702 refer to the emission from the target area (Fig. 1 and Fig. 3a) scaled over the entire DDS. This was
 703 possible by elaborating the data of the 30 campaigns reported in (Cardellini et al., 2017). From
 704 these data we computed the mean ratio between the DDS emission and that from the target area
 705 (4.7 ± 1.1), that is used as correction factor (error bars refer to the standard deviation of the
 706 correction factor)



708

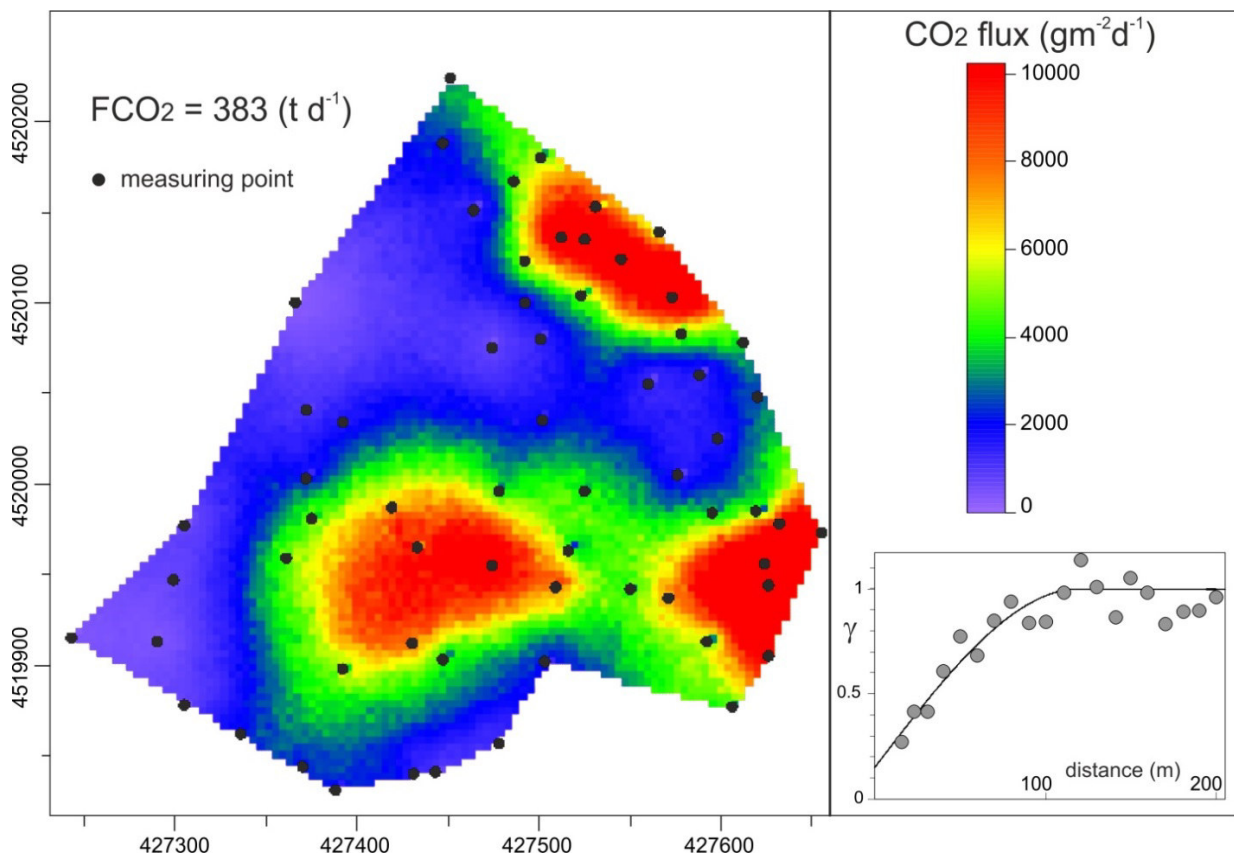
709

710 **Fig. 9.** Deep condensation rate and hydrothermal earthquakes occurrence. a) results of the steam
 711 mass balance involved in the degassing process (see the text); b) *Deep condensate* rate vs the
 712 monthly number of 'hydrothermal' earthquakes (grey histogram); c) normalized 'hydrothermal'
 713 earthquakes occurrence and normalized mean of deep condensate rate (six month values). See Fig. 7
 714 for the definition of 'hydrothermal' earthquakes.

715 **Supplementary Material**

716

717



718

719

720 **Supplementary Fig. S1.** Map of the mean CO₂ flux of the target area. The map was produced by
721 using the mean of the CO₂ fluxes measured in the 149 campaigns. In the figure is reported also the
722 experimental variogram of the normal score of the CO₂ flux and the corresponding variogram
723 model.

724

725 **Supplementary Data File S1.** Data sets: Bocca Nuova (BG) and Bocca Grande (BN) fumaroles
726 composition; soil CO₂ flux measurements at 63 locations in the Solfatara target area; total CO₂
727 output target area (FCO₂); Total CO₂ output form Solfatara DDS; CO₂ flux from Pisciarelli Vent;
728 RSAM at CPIS station; Air CO₂ concentration at Pisciarelli; 2004-2020 earthquakes.

729

730